



## Preparation and Characterization of (MCM-41)-Eu<sub>2</sub>O<sub>3</sub> Nanocomposite Materials

QING-ZHOU ZHAI\* and XIAO-DONG LI

Research Center for Nanotechnology, Changchun University of Science and Technology, 7186 Weixing Road, Changchun 130022, Jilin Province, P.R. China

\*Corresponding author: Fax: +86 431 85383815; Tel: +86 431 85583118; E-mail: zhaiqingzhou@163.com; zhaiqingzhou@hotmail.com

(Received: 21 February 2011;

Accepted: 14 October 2011)

AJC-10508

In the present study, a highly ordered mesoporous silica, nanoscale MCM-41, was synthesized and Eu<sub>2</sub>O<sub>3</sub> was successfully prepared into the channels of nanoscale MCM-41 via the following methods: liquid-phase grafting method, thermal diffusion method and microwave-assisted synthesis method. The luminescence of Eu<sup>3+</sup> is particularly interesting because Eu<sub>2</sub>O<sub>3</sub> is one of the most important rare earth oxides and the major emission band is centered near 618 nm (red), which is one of the three primary colours (red, blue and green) from which a wide spectrum of colours can be generated by appropriate mixing. The Eu<sup>3+</sup> ions show narrow emission bands arising from the <sup>5</sup>D<sub>J</sub> levels (J = 1, 2 and 3). Several characterization techniques were used to investigate physico-chemical properties of the prepared materials and to elucidate their luminescence properties. The prepared (MCM-41)-Eu<sub>2</sub>O<sub>3</sub> nanocomposite materials have the ordered hexagonal mesostructure of MCM-41 and show the properties of luminescence. The detailed luminescence studies of all the nanocomposite materials show that (MCM-41)-Eu<sub>2</sub>O<sub>3</sub> present stronger luminescent intensities and higher luminescent quantum efficiencies than bulk Eu<sub>2</sub>O<sub>3</sub>, indicating that the stability limitation of MCM-41 on the Eu<sub>2</sub>O<sub>3</sub> in the channels is a benefit for the luminescence properties of the (MCM-41)-Eu<sub>2</sub>O<sub>3</sub> nanocomposite materials. The emission spectra of (MCM-41)-Eu<sub>2</sub>O<sub>3</sub> display the characteristic luminescence of Eu<sub>2</sub>O<sub>3</sub> and the emission bands of (MCM-41)-Eu<sub>2</sub>O<sub>3</sub> in the long wavelength are <sup>5</sup>D<sub>0</sub> → <sup>7</sup>F<sub>J</sub> transitions of Eu<sub>2</sub>O<sub>3</sub> in the nanoscale MCM-41. It is believed that a markedly enhanced emission occurs owing to the strong interaction between Eu<sub>2</sub>O<sub>3</sub> and MCM-41. Meanwhile, the most effective preparative method (the microwave-assisted synthesis method) introduced in this paper is a very promising method for preparing (MCM-41)-Eu<sub>2</sub>O<sub>3</sub> nanocomposite materials.

**Key Words:** Nanocomposite materials, MCM-41, Europium oxide.

### INTRODUCTION

Since discovery of silica with a highly ordered mesoporous structure such as M41S<sup>1,2</sup>, many researchers have reported the potential applications of these materials having uniform pore structure and an extensively high surface area as catalysis, separation, adsorbent, drug delivery and guest-host chemical supports<sup>3-9</sup>. The most popular structures of these materials, mesoporous molecular sieve MCM-41, perform favourable uniformly and highly ordered network of silica with hexagonal pore diameter in the range of 2-50 nm. These outstanding characteristics such as large internal surface area, hexagonal array of one-dimensional cylindrical channels and high thermal stability result in various applications of MCM-41<sup>10-12</sup> and these properties make MCM-41 material among the best candidates as hosts for many guest materials<sup>13-18</sup> due to their good optical, thermal and chemical stability, especially for rare-earth oxide nanoparticles, which may prove useful in luminescence device applications. Recently, there has been considerable interest in the incorporation of the rare earth oxide in the mesoporous

materials for fundamental spectroscopic studies on luminescent properties and development of optical active materials<sup>19-21</sup>. The trivalent rare earth ions in oxide emit light at characteristic wavelengths due to intra 4f or inter 4f-5d transitions<sup>22</sup>. The 4f electrons of the rare earth ions are shielded by the outer 5s and 5p electrons. However, the intensities of 4f-4f transitions depend strongly on the nature and structure of chemical environment around the rare earth ions. Therefore, the key problem related to rare earth ions is to try to find a suitable matrix material and a proper method to load them. Up-to-date, several conventional strategies have been developed to incorporate rare earths nanoparticles in the channels of mesoporous silica MCM-41, SBA-15 and the pores of zeolites, including ion-exchange<sup>23,24</sup>, solid-state diffusion<sup>20,25</sup>, wetness impregnation<sup>26-28</sup>, co-condensation<sup>29,30</sup>, covalent grafting<sup>31-33</sup> and sol-gel<sup>34</sup> methods. Dai *et al.*<sup>35</sup>, synthesized cerium(III)-incorporated SBA-15 mesoporous molecular sieves by a two-step direct synthesis method in acid media. Trejda *et al.*<sup>36</sup>, applied a new synthesis route which allowed us to produce niobium-rich SBA-15 materials in which niobium was located exclusively in the

framework. Yada *et al.*<sup>37</sup>, described the rare earth (Er, Tm, Yb, Lu) oxide nanotubes templated by dodecyl sulfate assemblies. Different amounts of lanthanum oxide impregnated SBA-15 were synthesized and applied for arsenate removal in the adsorption process<sup>38</sup>. Ordered nanocrystalline mesoporous cerium oxide was synthesized using MCM-48 molecular sieves as a hard template<sup>39</sup>. Additionally, Tb<sup>3+</sup> and Eu<sup>3+</sup> have been doped in zeolite-Y,  $\beta$ -diketone modified SBA-15 or functionalized MCM-41 and novel photoluminescence and photophysical properties have been observed<sup>40-42</sup>.

Europium oxide is one of multifunctional rare earth oxides and has been studied extensively<sup>43-46</sup>. It is widely used as a red or blue phosphor in television sets and fluorescent lamps and as an activator for yttrium-based phosphors. It is also an agent for the manufacture of fluorescent glass. Europium fluorescence is used in the anticounterfeiting phosphors in Euro currency bank notes. Eu<sup>3+</sup> has a great advantage because the major emission band of Eu<sup>3+</sup> is centered near 620 nm<sup>47</sup>. Furthermore, Eu<sup>3+</sup> has non-degenerate ground and emitting states and the  $^5D_0 \rightarrow ^7F_0$  transition gives information about the site symmetry of host. This property permits possible application as structural probe of the local environment for technology of new optics sensors<sup>48</sup>. Now, a lot of studies are concentrated on the loading of rare earth oxides into the porous silica. Chen *et al.*<sup>20</sup> incorporated Eu<sub>2</sub>O<sub>3</sub> nanoparticles in the channels of MCM-41 by solid-state thermal diffusion at different temperatures and investigated the structure, luminescence and dynamics of Eu<sub>2</sub>O<sub>3</sub> nanoparticles in MCM-41. A coating of the internal surfaces of SBA-15 by rare earth oxides was impregnated by calcined host material with different aqueous rare earth nitrate solutions and subsequently calcined<sup>49</sup>.

Nanoscale MCM-41 is a novel mesoporous material synthesized in 2001<sup>50</sup>. In present work, the (MCM-41)-Eu<sub>2</sub>O<sub>3</sub> nanocomposite materials were successfully prepared *via* liquid-phase grafting method, thermal diffusion method and microwave-assisted synthesis method with a nanoscale MCM-41 as host. Generally, the conventional liquid-phase grafting method seems difficult to completely avoid adsorption of the nanoparticles on the outer surface of the MCM-41. Therefore, the surface of nanoscale MCM-41 is functionalized with organic groups by post synthesis method. However, the post synthesis method usually would destroy the framework of mesoporous materials, due to complicated synthetic process, rigorous preparing conditions and usage of solvent<sup>51-53</sup>. Furthermore, the nanoparticles easily deposit in the channel or aggregate on the external surface of mesoporous silica, which makes always the extra framework species form, irregularly distributes active sites and blocks the channel of mesoporous silica<sup>54</sup>. In order to overcome these shortcomings, the MCM-41 was modified by trimethylchlorosilane before calcination and the rare earth oxides should be incorporated into the modified MCM-41. The thermal diffusion method is applicable and effective procedure for the preparation of nanocomposites. Compared with the conventional liquid-phase grafting and thermal diffusion methods, microwave-assisted synthesis method has many advantages, such as fast crystallization, homogeneous nucleation and fast supersaturation by the rapid dissolution of precipitated gels<sup>55-58</sup>. It is also energy

efficient and economical. This method has been applied for the synthesis of several types of zeolites namely zeolite A, Y, ZSM-5, MCM-41, SBA-15<sup>55</sup>. To our best of knowledge, Eu<sub>2</sub>O<sub>3</sub> has not before been incorporated inside the channels of nanoscale MCM-41 using microwave-assisted synthesis method. Here, we successfully prepared nanocomposite of Eu<sub>2</sub>O<sub>3</sub> supported in nanoscale MCM-41 *via* liquid-phase grafting method, thermal diffusion method and microwave-assisted synthesis method. The structure and luminescent properties of (MCM-41)-Eu<sub>2</sub>O<sub>3</sub> nanocomposite materials were studied. We used chemical analysis, powder X-ray diffraction (XRD), Fourier transform infrared (FT-IR) spectra, low temperature N<sub>2</sub> adsorption-desorption technique at 77 K, high resolution transmission electron microscopy (HRTEM), environmental scanning electron microscopy (ESEM) and luminescence studies to characterize the prepared materials, whereas the most effective preparative method (the microwave-assisted synthesis method) introduced in this paper is a very promising method for preparing (MCM-41)-Eu<sub>2</sub>O<sub>3</sub> nanocomposite materials. The results showed that Eu<sub>2</sub>O<sub>3</sub> has been encapsulated inside the channels of nanoscale MCM-41 and the emissions of (MCM-41)-Eu<sub>2</sub>O<sub>3</sub> show a significant blue shift due to quantum size effect compared to that of the bulk Eu<sub>2</sub>O<sub>3</sub>. One of the main objectives of this work is to develop a novel preparation method for the (MCM-41)-Eu<sub>2</sub>O<sub>3</sub> and to investigate their luminescent properties.

## EXPERIMENTAL

Cetyltrimethylammonium bromide (CTMAB, Changzhou Xinhua Research Institute for Reagents, China), tetraethyl orthosilicate (TEOS, Sinopharm Chemical Reagent Co., Ltd, China), sodium hydroxide (Beijing Chemical Reagent Plant, China), trimethylchlorosilane (TMSCl, Sinopharmaceutical Chemical Reagent Co., Ltd, China), europium oxide (Sinopharmaceutical Chemical Reagent Co., Ltd, China), absolute ethanol (Beijing Chemical Reagent Plant, China), europium nitrate solutions were prepared from europium oxide and nitric acid. All reagents used in the experiment were of analytical grade. Deionized water was used throughout the experiments.

**Synthesis of MCM-41:** Nanoscale MCM-41 was prepared according to the procedure described by Cai *et al.*<sup>50</sup>. A 1 g of CTMAB was dissolved in 480 mL of deionized water at 80 °C under vigorous stirring until the solution became homogeneous. To this solution were added 3.5 mL of NaOH solution (2 mol L<sup>-1</sup>) with stirring. After the solution became homogeneous, 5 mL of TEOS was slowly dropped, giving rise to a white slurry. Then the reaction mixture was kept at 80 °C for 2 h with stirring. The resulting solid product was filtered, extensively washed with deionized water for three times and dried in air at room temperature to obtain the as-synthesized materials. The CTMAB surfactant molecules were then removed by calcination of the as-synthesized material at 550 °C in air for 4 h to obtain a white parent powder. The resulting product was afterwards designated as nanoscale MCM-41.

**Preparation of (MCM-41)-Eu<sub>2</sub>O<sub>3</sub> nanocomposite materials:** In the experiment the synthesis of (MCM-41)-Eu<sub>2</sub>O<sub>3</sub> nanocomposite materials includes three pathways: (I) The

modified MCM-41 was prepared on the basis of the method described in reference<sup>59</sup>. 0.5 g of uncalcined MCM-41 was immersed in 30 mL of 1 % (v/v) trimethylchlorosilane absolute ethanol solution and stirred at room temperature in air for 24 h. The resulting product was filtered off, washed with absolute ethanol solution and dried at 50 °C in air. The solid material was calcined at temperature 550 °C for 24 h and the modified MCM-41 was obtained. 0.3 g of modified MCM-41 was added into 30 mL of  $1.0 \times 10^{-2}$  mol L<sup>-1</sup> Eu(NO<sub>3</sub>)<sub>3</sub> solution at room temperature with stirring for 12 h. Then the resulting product was extensively washed with deionized water and dried at ambient temperature. Finally, the prepared material was heated at 500 °C for 3 h. The sample was designed as S1 (liquid phase grafting method loaded Eu<sub>2</sub>O<sub>3</sub> into the modified MCM-41). Similarly, 0.3 g of unmodified MCM-41 was added into 30 mL of  $1.0 \times 10^{-2}$  mol L<sup>-1</sup> Eu(NO<sub>3</sub>)<sub>3</sub> solution at room temperature with stirring for 12 h. Then the resulting product was collected by filtration, washed with deionized water and dried at room temperature. Finally, the prepared material was heated at 500 °C for 3 h. The sample was designed as S2 (liquid phase grafting method loaded Eu<sub>2</sub>O<sub>3</sub> into the unmodified MCM-41). (II) The formation of Eu<sub>2</sub>O<sub>3</sub> in the channels of MCM-41 was conducted by solid-state thermal diffusion, 0.5 g of MCM-41 was mixed with 0.0252 g of Eu<sub>2</sub>O<sub>3</sub> powder to make the mixture homogeneous, the mixed powders were heated at 150 and 500 °C for 5 h, respectively. Then, the samples were cooled down to room temperature in an oven and the solid phase thermal diffusion products were gotten. The samples were designed as S3 (solid-phase thermal diffusion at 150 °C) and S4 (solid-phase thermal diffusion at 500 °C). (III) 0.5 g of MCM-41 was mixed with 0.0252 g Eu<sub>2</sub>O<sub>3</sub> to make the mixture homogeneous. The mixture was irradiated by microwave for 0.5 h at 750 W in a microwave oven, subsequently, the sample was cooled down to room temperature in the oven. The sample was designed as S5 (microwave-assisted synthesis method). The host-guest nanocomposite materials were stored without air.

**Characterization:** The content of Eu<sub>2</sub>O<sub>3</sub> in samples was determined on a Hitachi Z-8000 polarization Zeeman atomic absorption spectrometer. Powder X-ray diffraction (XRD) patterns were obtained on Bruker D8/ADVANCE diffractometer with CuK<sub>α</sub> radiation (40 kV, 40 mA). The framework of MCM-41 was observed at low angles ( $1^\circ < 2\theta < 10^\circ$ ) and wide angles ( $10^\circ < 2\theta < 90^\circ$ ). Fourier transform infrared (FT-IR) spectra were recorded on an American Nicolet 5DX-FTIR spectrometer with potassium bromide pellets (99 wt. % of KBr). Low temperature nitrogen adsorption and desorption isotherms were obtained at 77 K on a Micromeritics ASAP 2020 V3.01 H volumetric analyzer (The American Mike Company). The samples were outgassed at 363 K prior to the measurements. The data were calculated in terms of the model of Bdb (Broekhoff and de Boer) method<sup>60</sup>. Surface area and pore volume were calculated by following BET<sup>61</sup> and BJH<sup>62</sup> procedures, respectively. High resolution transmission electron microscopic (HRTEM) images experiments were performed on a FEI Tecnai G2 F20 field-emission transmission microscope (Netherlands) operating at 200 kV. The samples were prepared by dispersing the powders in absolute ethanol.

Imaging was enabled by depositing a few drops of suspension on carbon coated 400 mesh Cu grid. The solvent was allowed to evaporate before imaging. Environmental scanning electron microscopic (ESEM) images were taken on a PHILIPS XL30 field-emission environmental scanning electron microscope (Netherlands) instrument. The surface distribution of elements was measured utilizing an energy dispersive X-ray (EDX) detector Genesis 2000 from EDAX (USA). Luminescence spectra were collected on a Hitachi F-7000 spectrophotometer (Japan) at room temperature of 20 °C, using a 150 W xenon lamp as the excitation source.

## RESULTS AND DISCUSSION

The percentages of Eu<sub>2</sub>O<sub>3</sub> in different samples were measured by chemical analysis and their contents were 1.54 % for S1, 1.57 % for S2, 4.76 % for S3, 4.76 % for S4 and 4.76 % for S5 in mass, respectively. It can be seen that Eu<sub>2</sub>O<sub>3</sub> has been incorporated into the (MCM-41)-Eu<sub>2</sub>O<sub>3</sub> nanocomposite materials.

The small-angle X-ray diffraction patterns (SAXRD) of the (MCM-41)-Eu<sub>2</sub>O<sub>3</sub> and corresponding nanoscale MCM-41 are displayed in Fig. 1. Nanoscale MCM-41 exhibits four well-resolved peaks that can be indexed as (100), (110), (200) and (210) reflections associated with a two-dimensional order hexagonal (space group p6mm) structure<sup>1,2</sup>. For the (MCM-41)-Eu<sub>2</sub>O<sub>3</sub> sample, one very strong and two weak characteristic peaks of MCM-41 material are clearly observed, which indicates that the hexagonal structure of the nanoscale MCM-41 in the composite material has been well maintained after the above synthesis process. However, the intensities of the (100), (110) and (200) reflections for (MCM-41)-Eu<sub>2</sub>O<sub>3</sub> are considerably reduced compared with the corresponding ones of peaks of the MCM-41 and the peak indexed to 210 diffraction disappeared, suggesting gradually lowering of long-range order of the samples. The results are consistent with the successful encapsulation of the Eu<sub>2</sub>O<sub>3</sub> within the channels of SBA-15 and suggest the presence of significant host-guest interaction<sup>63</sup>.

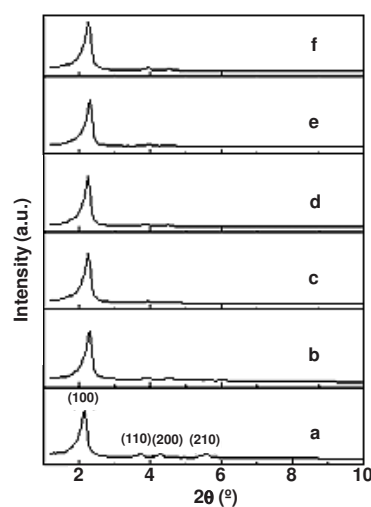


Fig. 1. Small-angle XRD patterns of (a) nanoscale MCM-41, (b) S1 (liquid phase grafting for modified MCM-41), (c) S2 (liquid phase grafting for unmodified MCM-41), (d) S3 (thermal diffusion at 150 °C), (e) S4 (thermal diffusion at 500 °C), (f) S5 (microwave-assisted synthesis)

Fig. 2 shows the wide-angle X-ray diffraction patterns of prepared samples. As no distinguishable peak was found, the pure nanoscale MCM-41 is amorphous. No reflections of  $\text{Eu}_2\text{O}_3$  are visible in the wide angle region for S1 and S2 samples (curve d, e), which suggests that the resultant  $\text{Eu}_2\text{O}_3$  introduced during the synthesis was located in the walls of the nanoscale MCM-41 or that crystalline  $\text{Eu}_2\text{O}_3$  species were very well dispersed in the channels. Hence, the  $\text{Eu}_2\text{O}_3$  cannot be detected with XRD. As observed in curve c, the characteristic reflection peaks of  $\text{Eu}_2\text{O}_3$  are represented for the mechanical mixture of nanoscale MCM-41 and  $\text{Eu}_2\text{O}_3$ . After heat treatment at  $150^\circ\text{C}$  (curve f) the peaks of  $\text{Eu}_2\text{O}_3$  still appear. However, it is of interest to note that the characteristic peaks assigned to  $\text{Eu}_2\text{O}_3$  disappear completely when the sample was heated at  $500^\circ\text{C}$  for 5 h (S4) or irradiated by microwave for 0.5 h (S5), as given in curve g or curve h. The phenomenon might be explained by high dispersion of  $\text{Eu}_2\text{O}_3$  into the channels of the nanoscale MCM-41, where the  $\text{Eu}_2\text{O}_3$  no longer exists in bulk state.

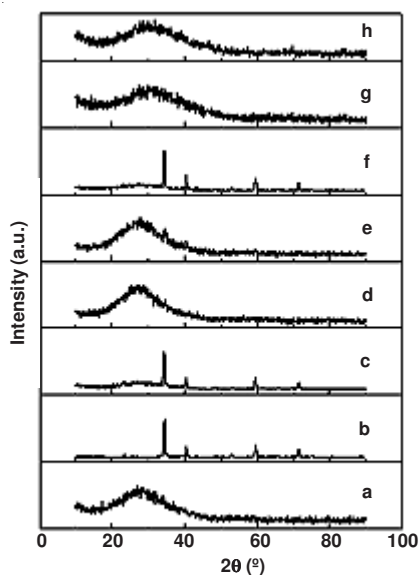


Fig. 2. Wide-angle XRD patterns of (a) nanoscale MCM-41, (b)  $\text{Eu}_2\text{O}_3$ , (c) mechanical mixture of nanoscale MCM-41 and  $\text{Eu}_2\text{O}_3$  (5 wt %), (d) S1 (liquid phase grafting for modified MCM-41), (e) S2 (liquid phase grafting for unmodified MCM-41), (f) S3 (thermal diffusion at  $150^\circ\text{C}$ ), (g) S4 (thermal diffusion at  $500^\circ\text{C}$ ), (h) S5 (microwave-assisted synthesis)

Fig. 3 shows the FT-IR spectra of all samples in the range  $2000\text{--}400\text{ cm}^{-1}$ . Curve b corresponds to the spectrum of nanoscale MCM-41 and curve c, d, e, f, g are the infrared spectra of (MCM-41)- $\text{Eu}_2\text{O}_3$ . The Si-O-Si vibrations appear as a very strong band at  $1080\text{ cm}^{-1}$  (asymmetric stretching), the peak at  $799\text{ cm}^{-1}$  can be attributed to the symmetric Si-O stretching vibration. The strong Si-O-Si bending vibration can be observed at  $460\text{ cm}^{-1}$  and the band at  $960\text{ cm}^{-1}$  can be assigned to stretching vibration of Si-OH surface group. In addition, the peak at  $1650\text{ cm}^{-1}$  can be attributed to the O-H bending vibration mode of the adsorbed water molecules. All bands in (MCM-41)- $\text{Eu}_2\text{O}_3$  samples show a shift to higher wavenumbers with respect to those of nanoscale MCM-41 molecular sieve.

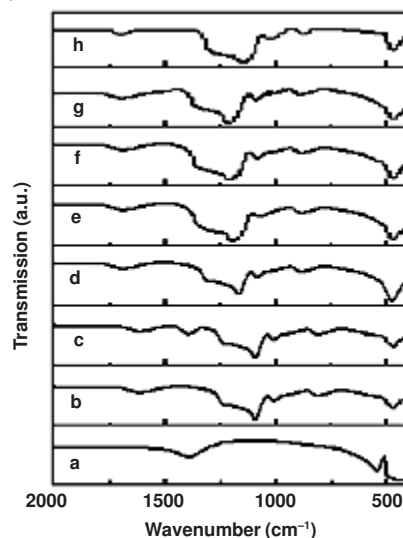


Fig. 3. Infrared spectra of (a)  $\text{Eu}_2\text{O}_3$ , (b) nanoscale MCM-41, (c) mechanical mixture of nanoscale MCM-41 and  $\text{Eu}_2\text{O}_3$  (5 wt %), (d) S1 (liquid phase grafting for modified MCM-41), (e) S2 (liquid phase grafting for unmodified MCM-41), (f) S3 (thermal diffusion at  $150^\circ\text{C}$ ), (g) S4 (thermal diffusion at  $500^\circ\text{C}$ ), (h) S5 (microwave-assisted synthesis)

This shift of the peaks is considered as an indication of the  $\text{Eu}_2\text{O}_3$  nanoparticles incorporated into the MCM-41<sup>64,65</sup>. Meanwhile, the FT-IR spectrum of bulk  $\text{Eu}_2\text{O}_3$  sample (curve a) has two peaks at about  $1400\text{ cm}^{-1}$ . For the mechanical mixture of nanoscale MCM-41 and  $\text{Eu}_2\text{O}_3$  (5 wt %) (curve c), the characteristic peaks of  $\text{Eu}_2\text{O}_3$  appear. However, no characteristic peaks of  $\text{Eu}_2\text{O}_3$  emerged in the infrared spectra of (MCM-41)- $\text{Eu}_2\text{O}_3$  samples, showing that  $\text{Eu}_2\text{O}_3$  has already been entrapped in nanochannels of the MCM-41 and equally dispersed on the surface of nanoscale MCM-41 but not simply doped or physically absorbed outside.

Nitrogen adsorption-desorption is a technique to assess the textures of pore materials. Fig. 4 shows the low-temperature  $\text{N}_2$  adsorption-desorption isotherms of samples at  $77\text{ K}$ . All samples exhibit reversible type Langmuir IV isotherm with the presence of two hysteresis loops<sup>66,67</sup>. The H1 hysteresis loop in Fig. 4 showed that the materials are typical of mesoporous materials. The structure data of different (MCM-41)- $\text{Eu}_2\text{O}_3$  nanocomposite materials, extracted from the adsorption isotherms, are summarized in Table-1. The results reveal that the doping of  $\text{Eu}_2\text{O}_3$  has not altered the basic pore structure of mesoporous MCM-41. A linear increase in adsorbed volume at low pressures was followed by a steep increase in nitrogen uptake at a relative pressure  $0.3 < P/P_0 < 0.4$ , which was due to the uniformity of the mesoporous size distribution and capillary condensation inside the mesopore at a characteristic relative pressure<sup>68,69</sup>. The position of the inflection point is clearly related to the diameter of the mesopore range and the sharpness of this step suggested the good distribution of the  $\text{Eu}_2\text{O}_3$  in the channels of the host molecular sieves<sup>70-72</sup>. When the relative pressure is  $0.4 < P/P_0 < 0.9$ , all isotherms have a gentle slope. The adsorption of  $\text{N}_2$  at the surface of the pore channels reaches an equilibrium, which exhibits a long well defined plateau. Subsequently, the adsorption-desorption isotherms exhibit well defined hysteresis loops at a relative pressure  $0.9 < P/P_0 < 1.0$  due to the existence

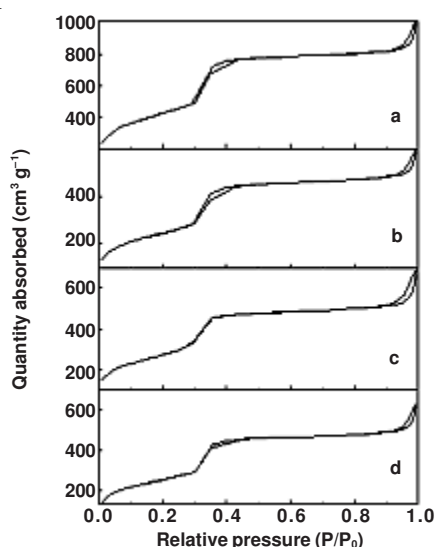


Fig. 4. Low-temperature nitrogen adsorption-desorption isotherms of (a) nanoscale MCM-41, (b) S1 (liquid phase grafting for modified MCM-41), (c) S4 (thermal diffusion at 500 °C), (d) S5 (microwave-assisted synthesis)

TABLE-1  
PORE STRUCTURE PARAMETERS OF SAMPLES

Samples	$d_{100}$ (nm)	$a_0^a$ (nm)	BET surface area (m <sup>2</sup> /g)	Pore volume <sup>b</sup> (cm <sup>3</sup> /g)	Pore size <sup>c</sup> (nm)
Nanometer MCM-41	3.34	3.85	1329	1.33	3.55
S1	3.85	4.44	996	0.85	3.52
S4	3.84	4.43	893	0.80	3.33
S5	3.91	4.51	902	0.81	3.36

<sup>a</sup>  $a_0 = \frac{2}{\sqrt{3}} d_{100}$  <sup>b</sup>BJH adsorption cumulative volume of pores. <sup>c</sup>Pore size calculated from the adsorption branch.

of noticeable amount of large irregular pores between silica particles. In the last case the pronounced capillary condensation steps occur at about  $P/P_0 = 0.9$  when the capillary condensation of nitrogen gas in regular and granular pores is completed. The hysteresis loop was closely related to the degree of order and the expedite channel structure in samples. Therefore, as the order degree of samples decreases, the hysteresis loop tend to disappear at relative lower pressures, which can be attributed to the reduced pore volume and the condensation in the adsorption branch starting at lower  $P/P_0$  is caused by the smaller pore size. This implies that part of the pore space has been occupied during the modification of the pore surface and most of the pores were then filled up by inclusion of Eu<sub>2</sub>O<sub>3</sub> into the pores (curve b). However, the hysteresis in high pressures corresponds to the mesoporosity character of MCM-41, confirming that Eu<sub>2</sub>O<sub>3</sub> particles have been properly confined inside the pore channels of nanoscale MCM-41 for all samples and the mesoporous channels still have been remained.

Fig. 5 presents pore size distributions (PSDs). The three curves of the samples are close to a Gaussian distribution and the very narrow pore size distributions peaks are observed for all samples, which suggests high uniformity of pore dimensions. However, the  $S_{BET}$ , the pore size distributions and the pore volumes were decreased with the incorporation of the Eu<sub>2</sub>O<sub>3</sub> particles. Consequently, the guest Eu<sub>2</sub>O<sub>3</sub> in form of large

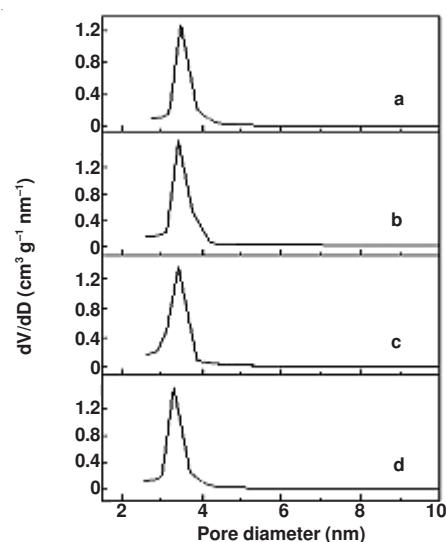


Fig. 5. Pore size distribution patterns of samples: (a) nanoscale MCM-41, (b) S1 (liquid phase grafting for modified MCM-41), (c) S4 (thermal diffusion at 500 °C), (d) S5 (microwave-assisted synthesis)

particles was partially located inside the MCM-41 pores while blocking the pores significantly. Compared with the other samples, the S5 synthesized by microwave diffusion has lower BET surface area, indicating that the guest Eu<sub>2</sub>O<sub>3</sub> particles relatively homogeneously cover the internal surface of the MCM-41. The structure information about the samples derived from nitrogen adsorption-desorption data are listed in Table-1.

For calculating the blockage effect of Eu<sub>2</sub>O<sub>3</sub> on the channels of the MCM-41 molecular sieve quantitatively, in this study the normalized surface area of materials (NSA)<sup>73</sup> was calculated. According to the NSA value of material the state of guest in the composite materials can be determined as follows (Fig. 6)<sup>73</sup>: (1) When the NSA of composite material is  $\ll 1$ , the guest material will form relatively larger particles (Fig. 6A). These particles enter the channels of the molecular sieve, blocking the channels, making the pore volume, surface area and pore size of molecular sieve dramatically smaller. (2) When the NSA of composite material is approximately equals to 1, the guest material will form a noncrystal layer, closely covering inner surface of the molecular sieve (Fig. 6B). Because these particles attached to inner surface of the molecular sieve form a new surface, it only covers the original surface. Thus, the NSA value of this type is close to 1. (3) When the NSA of composite material is  $> 1$ , the guest material will become very small nanocrystals. It disperses on the internal and external surface of the molecular sieve (Fig. 6C), because the size of these nanocrystals is very small, making a significant increase of surface area in the composite material. So the NSA is much larger than 1.

The formula of normalized surface area (NSA) is as follows<sup>73</sup>:

$$NSA = \frac{SA_1}{1-y} \times \frac{1}{SA_2}$$

$SA_1$  and  $SA_2$  are the surface area of (MCM-41)-Eu<sub>2</sub>O<sub>3</sub> nanocomposite materials and the original MCM-41 molecular sieve powder, respectively,  $y$  is mass fraction of the Eu<sub>2</sub>O<sub>3</sub> in the composite material.

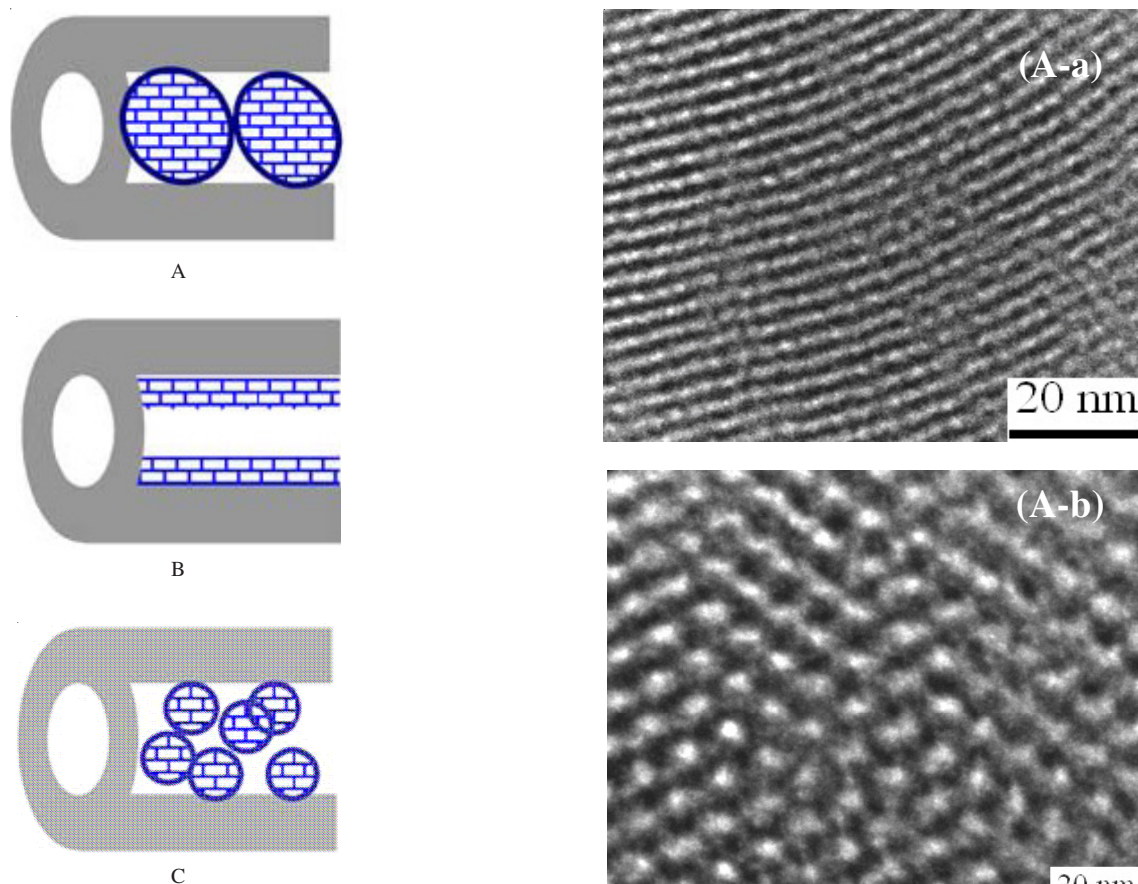


Fig. 6. Guest phase assembling inside the MCM-41. (A) type I; (B) Type II; (C) Type III [Ref. 73]

In the present study, the NSA values of the S1, S4 and S5 samples are 0.71, 0.82 and 0.73 from the NSA values of the samples, respectively. We can see that the NSA values of the (MCM-41)- $\text{Eu}_2\text{O}_3$  samples are approximately equals to 1. Therefore,  $\text{Eu}_2\text{O}_3$  particles formed noncrystalline layer in the (MCM-41)- $\text{Eu}_2\text{O}_3$  samples. This made pore volume, surface area and pore size of the molecular sieve smaller. These results and the nitrogen adsorption-desorption isotherms results are consistent.

**High resolution transmission electron microscopy images:** The homogeneity of the distribution of  $\text{Eu}_2\text{O}_3$  particles and its influence on the well-ordered hexagonal array of MCM-41 are further confirmed from the high resolution transmission electron microscopic (HRTEM) images (Fig. 7). The ordered mesoporous structure of nanoscale MCM-41 is confirmed by HRTEM in Fig. 7A, which clearly displays a worm-hole pore structure with a narrow average pore diameter of 3.5 nm. The uniformly well-ordered nanosized channels (about 3-5 nm) separated by silica walls are packed regularly in a hexagonal manner. Fig. 7B-E show some representative images of (MCM-41)- $\text{Eu}_2\text{O}_3$  taken from distinct specimens, where the highly ordered pore structures of MCM-41 are still preserved. The parallel straight channels (Fig. 7-b) can be observed with the incident electron beam perpendicular to the channels. When observed with the incident beam parallel to the channels, as shown in Fig. 7a, the (MCM-41)- $\text{Eu}_2\text{O}_3$  nanocomposite shows the highly ordered honeycomb-like pore array structure. The average thickness of the wall is 3-5 nm and the pore diameter is

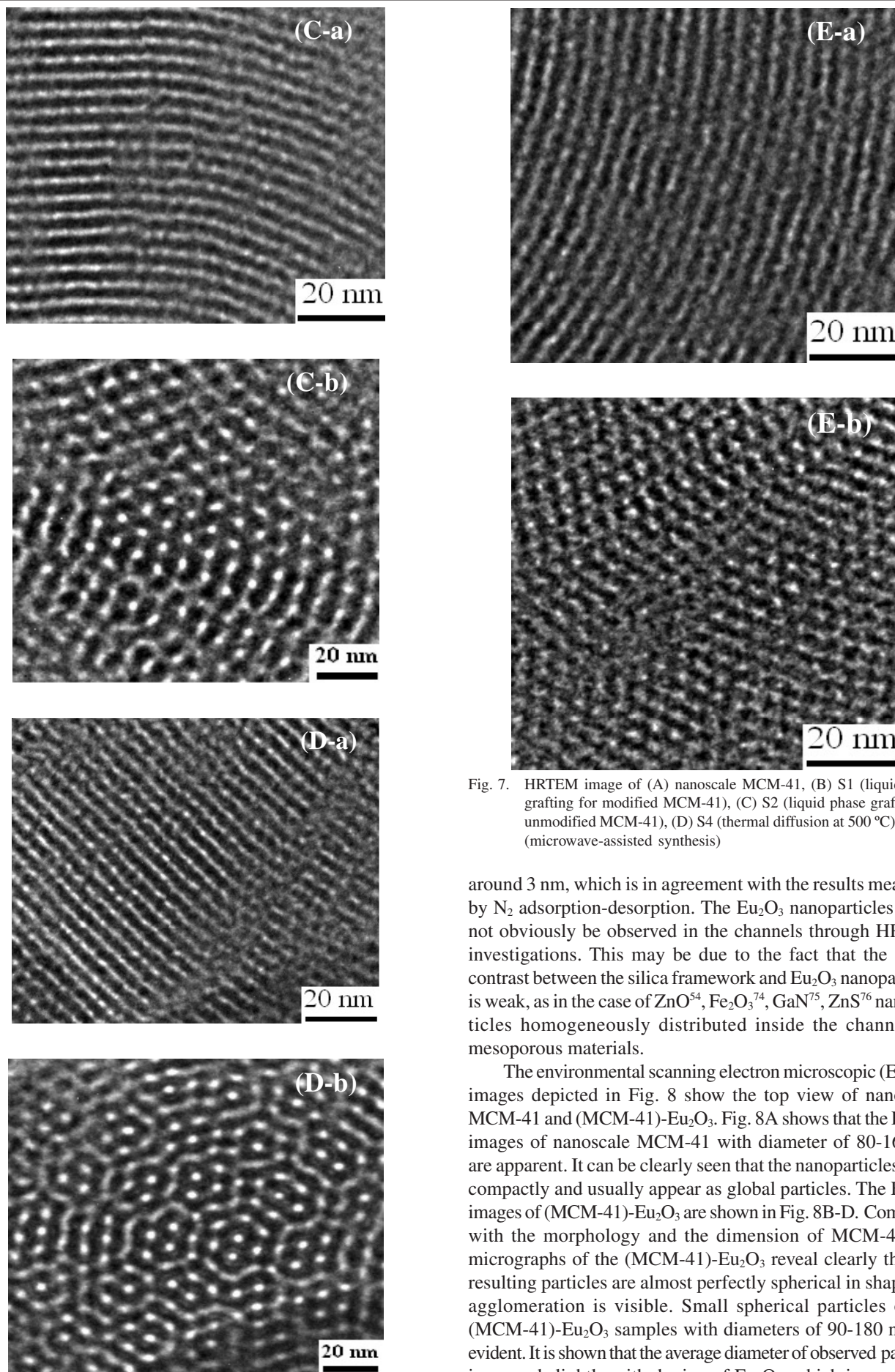


Fig. 7. HRTEM image of (A) nanoscale MCM-41, (B) S1 (liquid phase grafting for modified MCM-41), (C) S2 (liquid phase grafting for unmodified MCM-41), (D) S4 (thermal diffusion at 500 °C), (E) S5 (microwave-assisted synthesis)

around 3 nm, which is in agreement with the results measured by N<sub>2</sub> adsorption-desorption. The Eu<sub>2</sub>O<sub>3</sub> nanoparticles could not obviously be observed in the channels through HRTEM investigations. This may be due to the fact that the image contrast between the silica framework and Eu<sub>2</sub>O<sub>3</sub> nanoparticles is weak, as in the case of ZnO<sup>54</sup>, Fe<sub>2</sub>O<sub>3</sub><sup>74</sup>, GaN<sup>75</sup>, ZnS<sup>76</sup> nanoparticles homogeneously distributed inside the channels of mesoporous materials.

The environmental scanning electron microscopic (ESEM) images depicted in Fig. 8 show the top view of nanoscale MCM-41 and (MCM-41)-Eu<sub>2</sub>O<sub>3</sub>. Fig. 8A shows that the ESEM images of nanoscale MCM-41 with diameter of 80-160 nm are apparent. It can be clearly seen that the nanoparticles stack compactly and usually appear as global particles. The ESEM images of (MCM-41)-Eu<sub>2</sub>O<sub>3</sub> are shown in Fig. 8B-D. Compared with the morphology and the dimension of MCM-41, the micrographs of the (MCM-41)-Eu<sub>2</sub>O<sub>3</sub> reveal clearly that the resulting particles are almost perfectly spherical in shape. No agglomeration is visible. Small spherical particles of the (MCM-41)-Eu<sub>2</sub>O<sub>3</sub> samples with diameters of 90-180 nm are evident. It is shown that the average diameter of observed particles increased slightly with doping of Eu<sub>2</sub>O<sub>3</sub>, which is consistent

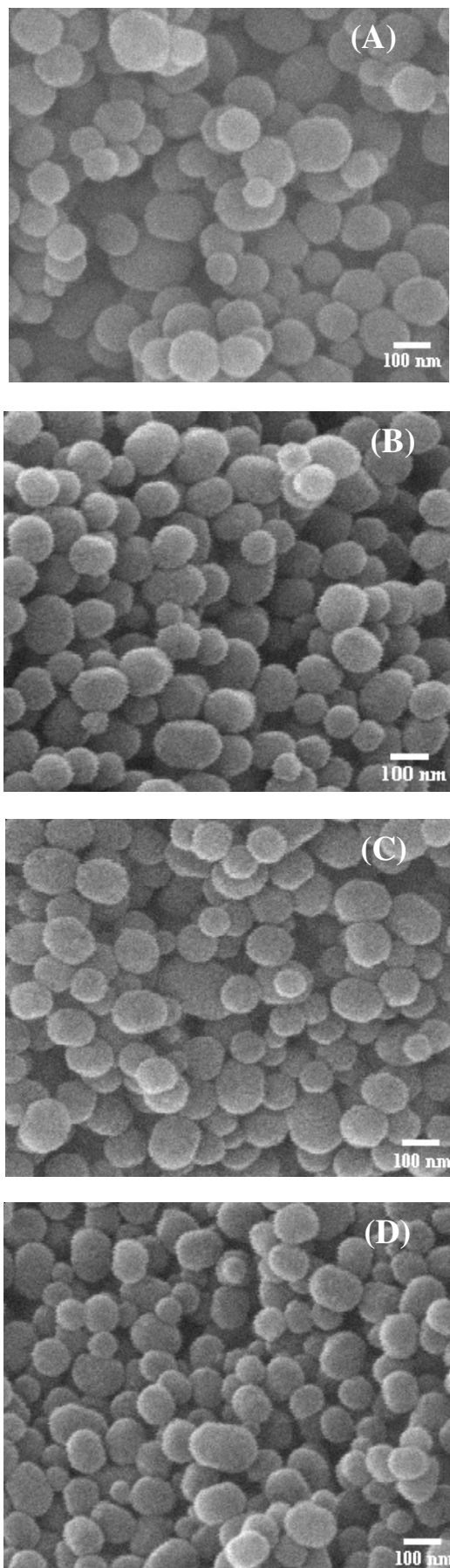


Fig. 8. ESEM image of (A) nanoscale MCM-41, (B) S1 (liquid phase grafting for modified MCM-41), (C) S4 (thermal diffusion at 500 °C), (D) S5 (microwave-assisted synthesis)

with the data of XRD and N<sub>2</sub> adsorption-desorption. Furthermore, the existence of the rare earth oxide in the coated or doped materials was examined by the energy dispersive X-ray (EDX) measurements. The EDX spectrum serves also as a rough estimate for the quantitative determination of the rare earth atoms. A typical spectrum of S5 is presented in Fig. 9. It shows that Eu element existed inside the pore channels of nanoscale MCM-41. As the high surface area of MCM-41 molecular sieve is mainly due to its nanoscale pore channels, thus the abundant Eu<sub>2</sub>O<sub>3</sub> particles should be homogeneously distributed in the pores of nanoscale MCM-41.

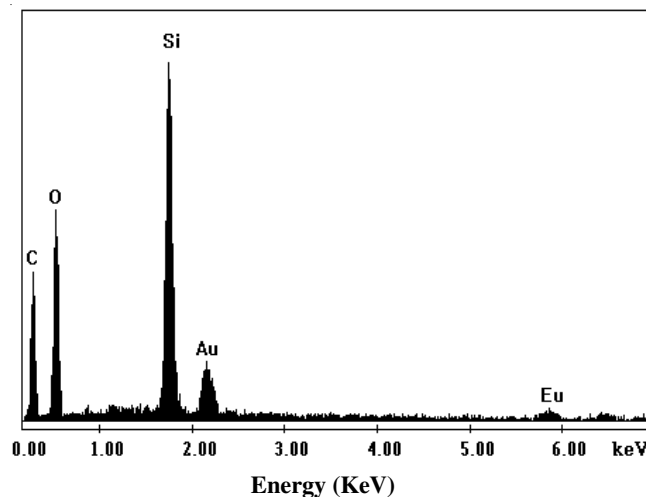


Fig. 9. EDX pattern of S5

Fig. 10 shows the luminescence spectra of Eu<sub>2</sub>O<sub>3</sub> and the (MCM-41)-Eu<sub>2</sub>O<sub>3</sub> nanocomposites at room temperature under the same experimental conditions. We observed the emission of Eu<sub>2</sub>O<sub>3</sub> corresponding to the <sup>5</sup>D<sub>0</sub> → <sup>7</sup>F<sub>J</sub> (*J* = 0, 1, 2, 3, 4) transitions in the range of 500-700 nm (curve a), which show strong inhomogeneous broadening indicative of an amorphous oxide environment<sup>77</sup>. Their narrow emission lines have low intensity, because they are parity and spin forbidden. The oscillator strengths of absorption to the excited states of Eu<sup>3+</sup> ions, as for other rare earth ions, are of the order of magnitude 10<sup>-5</sup>-10<sup>-6</sup>. The emission spectra of rare earth ions arise from transitions within the 4*f* shell and the <sup>5</sup>D<sub>0</sub> → <sup>7</sup>F<sub>J</sub> emission is most suitable for surveying the transition probabilities of sharp spectral features in rare earths. If a rare-earth ion occupies a site with inversion symmetry in a crystal lattice, the optical transitions between 4*f* levels are strictly forbidden as electric-dipole transitions, which obeys the selection rule Δ*J* = 0, ±1 (*J* = 0 to *J* = 0 being forbidden) or as vibronic electric dipole transitions. As shown in curve a, the emission (618 nm) corresponding to the <sup>5</sup>D<sub>0</sub> → <sup>7</sup>F<sub>2</sub> electric dipole transition of Eu<sup>3+</sup> is predominantly observed. The emission at 595 nm is considered to be the <sup>5</sup>D<sub>0</sub> → <sup>7</sup>F<sub>1</sub> magnetic-dipole allowed transition of Eu<sup>3+</sup>. The emission peak at 580 nm is assigned to the <sup>5</sup>D<sub>0</sub> → <sup>7</sup>F<sub>0</sub> transition of Eu<sup>3+</sup>. The weak emission peak is at 633 nm, which belongs to the <sup>5</sup>D<sub>0</sub> → <sup>7</sup>F<sub>3</sub> transition. In curve b, the spectrum of mechanical mixture of nanoscale MCM-41 and Eu<sub>2</sub>O<sub>3</sub> (5 wt %) was similar as that of the Eu<sub>2</sub>O<sub>3</sub>. Moreover, the <sup>5</sup>D<sub>0</sub> → <sup>7</sup>F<sub>2</sub> also has the strongest emission intensity in the spectrum of the mechanical mixture of MCM-41 and Eu<sub>2</sub>O<sub>3</sub>. For comparison,

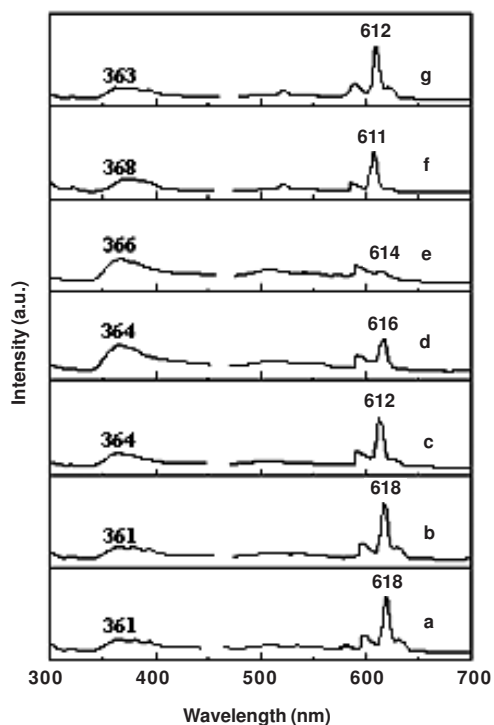


Fig. 10. Luminescence spectra of: (a) Eu<sub>2</sub>O<sub>3</sub>, (b) mechanical mixture of nanoscale MCM-41 and Eu<sub>2</sub>O<sub>3</sub> (5 wt %), (c) S1 (liquid phase grafting for modified MCM-41), (d) S2 (liquid phase grafting for unmodified MCM-41), (e) S3 (thermal diffusion at 150 °C), (f) S4 (thermal diffusion at 500 °C), (g) S5 (microwave-assisted synthesis)

emission spectra of the Eu<sub>2</sub>O<sub>3</sub> in the modified and unmodified MCM-41 are presented in curve c and d. Both spectra show the characteristic emission bands of Eu<sup>3+</sup>. However, the luminescence intensity of <sup>5</sup>D<sub>0</sub> → <sup>7</sup>F<sub>2</sub> of the Eu<sub>2</sub>O<sub>3</sub> in the modified MCM-41 (curve c) is about 3 times stronger than that in the unmodified MCM-41 (curve d), showing that the Eu<sub>2</sub>O<sub>3</sub> particles were mostly incorporated in the channels of modified MCM-41. Therefore, the decrease of the non-radiative transition ratio, the luminescence intensity increases<sup>78,79</sup>. In addition, the broadening <sup>5</sup>D<sub>0</sub> → <sup>7</sup>F<sub>2</sub> emission peak of S3 at 614 nm decreases in intensity, which is due to a charge transfer transition. -OH groups also can lead to vibrational deexcitation, to which Eu<sup>3+</sup> is highly susceptible.

The <sup>5</sup>D<sub>0</sub> → <sup>7</sup>F<sub>2</sub> transition is highly sensitive to structural change and environmental effects. Therefore, the higher temperature (500 °C) enhanced the activity of Eu<sup>3+</sup> and the stronger interaction of electron-photon in S4 induced the increase in intensity of the <sup>5</sup>D<sub>0</sub> → <sup>7</sup>F<sub>2</sub> emission peak of S4. In the curve f and g, the wide bands centered in 520 nm were observed, which were attributed to the oxygen vacancy in the silicon tetrahedron, as well as to the presence of superficial defects in the structure of MCM-41. It is worth noting that the characteristic emission lines are still obvious in the emission spectrum for S5 (curve g), the two main characteristic peaks of S5 from <sup>5</sup>D<sub>0</sub> → <sup>7</sup>F<sub>1</sub> (590 nm) and <sup>5</sup>D<sub>0</sub> → <sup>7</sup>F<sub>2</sub> (612 nm) are dominant. The <sup>5</sup>D<sub>0</sub> → <sup>7</sup>F<sub>2</sub> transition is a typical electric dipole transition and strongly varies with the local symmetry of Eu<sup>3+</sup> ions, while the <sup>5</sup>D<sub>0</sub> → <sup>7</sup>F<sub>1</sub> transition corresponds to a parity-allowed magnetic dipole transition, which is practically independent of the host material<sup>23</sup>. Therefore, the intensity ratio (R) of <sup>5</sup>D<sub>0</sub> → <sup>7</sup>F<sub>2</sub> to

<sup>5</sup>D<sub>0</sub> → <sup>7</sup>F<sub>1</sub> is sensitive to the symmetry around Eu<sup>3+</sup> ions and gives valuable information about environment change<sup>80</sup>. When the R value is higher, the Eu<sup>3+</sup> ions occupy sites of lower symmetry without inversion center (more asymmetric local environment). Therefore, the fact suggests that the local symmetry changed as the Eu<sub>2</sub>O<sub>3</sub> was incorporated into the channels of nanoscale MCM-41 and indicates the occupation of the Eu<sup>3+</sup> in silica mesopore in low symmetric environment, probably due to the effect of confinement and some defects on the surface of nanoscale MCM-41. Otherwise, it is possible that the formation of unilayer enhances the Eu<sub>2</sub>O<sub>3</sub>-MCM-41 distance. The energy transfer between the MCM-41 and the Eu<sup>3+</sup> is a nonradiative process, which would account for the increase of the Eu<sub>2</sub>O<sub>3</sub> emission. Compared with the emission peak of bulk Eu<sub>2</sub>O<sub>3</sub> at 618 nm (curve a), the emission peaks of S1, S4 and S5 show the significant blue shift of 6, 7 and 6 nm relative to the emission peaks of 612, 611 and 612 nm. It is suggested that Eu<sub>2</sub>O<sub>3</sub> particles have grown inside the channels of MCM-41 and gave rise to the strongest quantum size effect. On the base of other reason, the blue shift behaviour can be attributed to the small size of Eu<sub>2</sub>O<sub>3</sub> particles, their large energy gap and the increase of energy of forbidden band. Hence, the blue shifting of the band gap dependent transition is typically characteristic of quantum confinement effect of the nanoscale Eu<sub>2</sub>O<sub>3</sub> brought about by the restricted pore sizes. Eu<sub>2</sub>O<sub>3</sub> is incorporated into the channels of nanoscale MCM-41 that made molecules of Eu<sub>2</sub>O<sub>3</sub> arrange tidily and kinetic energy decrease. The decreasing kinetic energy increases the luminescent intensities of the composite materials and peaks of the emission spectra move to the higher energy levels.

## Conclusion

In summary, the microwave-assisted synthesis method for synthesizing Eu<sub>2</sub>O<sub>3</sub> nanoparticles inside the pores of nanoscale MCM-41 has been reported. The samples exhibited emission bands at 618 and 590 nm from Eu<sup>3+</sup>. At the same time, the modified MCM-41 as host for the synthesis of (MCM-41)-Eu<sub>2</sub>O<sub>3</sub> was described. Moreover, direct incorporation of Eu<sub>2</sub>O<sub>3</sub> nanoparticles into the pores of nanoscale MCM-41 by thermal diffusion method provided various possibilities for fabricating novel nanocomposite, adjusting the temperature of the synthesis process is specially important. The Eu<sub>2</sub>O<sub>3</sub> were attached in the inner surfaces of the nanoscale MCM-41, which retains significant high ordered hexagonal mesostructure after the incorporation of Eu<sub>2</sub>O<sub>3</sub>. The preparation of (MCM-41)-Eu<sub>2</sub>O<sub>3</sub> by microwave-assisted synthesis method exhibited the characteristic luminescence property and higher luminescence quantum efficiency compared with other methods. An unusually intensified emission band occurred at 618 nm though a <sup>5</sup>D<sub>0</sub> → <sup>7</sup>F<sub>2</sub> electronic transition with Eu<sub>2</sub>O<sub>3</sub> nanoparticles embedded in nanoscale MCM-41 molecular sieves. An enhanced electron-phonon interaction could thus occur, which promoted the emission. It was proposed that the emission spectra display the characteristic emission peak of Eu<sup>3+</sup> ions through the intramolecular energy transfers from MCM-41 to Eu<sub>2</sub>O<sub>3</sub>. Furthermore, the channels of MCM-41 in the (MCM-41)-Eu<sub>2</sub>O<sub>3</sub> have the obvious quantum size effect on the nanoscale Eu<sub>2</sub>O<sub>3</sub>. The prepared (MCM-41)-Eu<sub>2</sub>O<sub>3</sub> nanocomposites have the potential application as luminescent materials.

## REFERENCES

- J.S. Beck, J.C. Vartuli, W.J. Roth, M.E. Leonowicz, C.T. Kresge, K.D. Schmitt, C.T.W. Chu, D.H. Olson, E.W. Sheppard, S.B. McCullen, J.B. Higgins and J.L. Schlenker, *J. Am. Chem. Soc.*, **114**, 10834 (1992).
- C.T. Kresge, M.E. Leonowicz, W.J. Roth, J.C. Vartuli and J.S. Beck, *Nature*, **359**, 710 (1992).
- A. Corma, *Chem. Rev.*, **97**, 2373 (1997).
- A.P. Wight and M.E. Davis, *Chem. Rev.*, **102**, 3589 (2002).
- K. Dimos, P. Stathi, M.A. Karakassides and Y. Deligiannakis, *Micropor. Mesopor. Mater.*, **126**, 65 (2009).
- N.K. Mal, M. Fujiwara and Y. Tanaka, *Nature*, **421**, 350 (2003).
- M. Vallet-Regi, A. Ramila, R.P. del Real and J. Perez-Pariente, *Chem. Mater.*, **13**, 308 (2001).
- Y. Wan, H.-F. Yang and D.-Y. Zhao, *Acc. Chem. Res.*, **39**, 423 (2006).
- S. Minakata, R. Tsuruoka and M. Komatsu, *J. Am. Chem. Soc.*, **130**, 1536 (2008).
- B. Coasne, F.R. Hung, R.J.M. Pellenq, F.R. Siperstein and K.E. Gubbins, *Langmuir*, **22**, 194 (2006).
- Y. Xiong, L.-Z. Zhang, G.-Q. Tang, G.-L. Zhang and W.-J. Chen, *J. Lumin.*, **110**, 17 (2004).
- F. Balas, M. Manzano, P. Horcajada and M. Vallet-Regi, *J. Am. Chem. Soc.*, **128**, 8116 (2006).
- M. Stockenhuber, M.J. Hudson and R.W. Joyner, *J. Phys. Chem. B*, **104**, 3370 (2000).
- L. Vradman, M.V. Landau, D. Kantorovich, Y. Koltypin and A. Gedanken, *Micropor. Mesopor. Mater.*, **79**, 307 (2005).
- A. Ramila, B. Munoz, J. Perez-Pariente and M. Vallet-Regi, *J. Sol-Gel Sci. Technol.*, **26**, 1199 (2003).
- K. Dimos, I.B. Koutselas and M.A. Karakassides, *J. Phys. Chem. B*, **110**, 22339 (2006).
- A. Pourahmad and S. Sohrabnezhad, *J. Alloys. Compd.*, **484**, 314 (2009).
- Q.-Q. Wang and D.F. Shantz, *J. Solid. State. Chem.*, **181**, 1659 (2008).
- K.R. Kloetstra, M. Van Laren and H. Van Bekkum, *Faraday Trans.*, **93**, 1211 (1997).
- W. Chen, A.G. Joly, C.M. Kowalchuk, J.O. Malm, Y.-N. Huang and J.O. Bovin, *J. Phys. Chem. B*, **106**, 7034 (2002).
- X.-L. Song, P. Qu, N. Jiang, H.-M. Yang and G.-Z. Qiu, *Colloids. Surf. A*, **313-314**, 193 (2008).
- R. Ternane, M. Trabelsi-Ayed, N. Kbir-Arighuib and B. Piriou, *J. Lumin.*, **81**, 165 (1999).
- X.-M. Guo, L.-S. Fu, H.-J. Zhang, L.D. Carlos, C.-Y. Peng, J.-F. Guo, J.-B. Yu, R.-P. Deng and L.-N. Sun, *New. J. Chem.*, **29**, 1351 (2005).
- Z. Lin, J.P. Rainho, J. Domingues, L.D. Carlos and J. Rocha, *Micropor. Mesopor. Mater.*, **79**, 13 (2005).
- J.K. Reddy, V.D. Kumari and M. Subrahmanyam, *Catal. Lett.*, **123**, 301 (2008).
- C.-X. Zhao, W. Chen, C. Wu and J. Zhou, *Nanotechnology*, **11**, 249 (2006).
- Y.-D. Bi, W. Zhang, H.-Y. Xu and W.-Z. Li, *Catal. Lett.*, **119**, 126 (2007).
- Z.-M. Tian, Q.-G. Deng, H. Sun and D.-F. Zhao, *Chem. Res. Chin. Univ.*, **24**, 357 (2008).
- Y.-P. Kuang, N.-Y. He, J. Wang, P.-F. Xiao, C.-W. Yuan and Z.-H. Lu, *Colloids. Surf. A*, **179**, 177 (2001).
- Y.G. Wang, L. Wang, H.-R. Li, P. Liu, D.-S. Qin, B.-Y. Liu, W.-J. Zhang, R.-P. Deng and H.-J. Zhang, *J. Solid. State. Chem.*, **181**, 562 (2008).
- X.-M. Guo, X.-M. Wang, H.-J. Zhang, L.-S. Fu, H.-D. Guo, J.-B. Yu, L.D. Carlos and K.-Y. Yang, *Micropor. Mesopor. Mater.*, **116**, 28 (2008).
- Y. Li and B. Yan, *J. Solid. State. Chem.*, **181**, 1032 (2008).
- C.-Y. Peng, H.-J. Zhang, J.-B. Yu, Q.-G. Meng, L.-S. Fu, H.-R. Li, L.-N. Sun and X.-M. Guo, *J. Phys. Chem. B*, **109**, 15278 (2005).
- Q.-Y. Zhang, K. Pita, W. Ye and W.-X. Que, *Chem. Phys. Lett.*, **351**, 163 (2002).
- Q.-G. Dai, X.-Y. Wang, G.-P. Chen, Y. Zheng and G.-Z. Lu, *Micropor. Mesopor. Mater.*, **100**, 268 (2007).
- M. Trejda, A. Tuel, J. Kujawa, B. Kilos and M. Ziolk, *Micropor. Mesopor. Mater.*, **110**, 271 (2008).
- M. Yada, M. Mihara, S. Mouri, M. Kuroki and T. Kijima, *Adv. Mater.*, **14**, 309 (2002).
- M. Jang, J.K. Park and E.W. Shin, *Micropor. Mesopor. Mater.*, **75**, 159 (2004).
- P.-F. Ji, J.-L. Zhang, F. Chen and M. Anpo, *J. Phys. Chem. C*, **112**, 17809 (2008).
- W. Chen, R. Sammynaiken and Y.N. Huang, *J. Appl. Phys.*, **88**, 1424 (2000).
- Y.-J. Li and B. Yan, *Inorg. Chem.*, **48**, 8276 (2009).
- Y. Li and B. Yan, *Micropor. Mesopor. Mater.*, **128**, 62 (2010).
- B.M. Tissue, *Chem. Mater.*, **10**, 2837 (1998).
- A. Patra, E. Sominska, S. Ramesh, Y. Koltypin, Z. Zhong, H. Minti, R. Reisfeld and A. Gedanken, *J. Phys. Chem. B*, **103**, 3361 (1999).
- L. Fu, Z.-M. Liu, Y.-Q. Liu, B.-X. Han, J.-Q. Wang, P.-A. Hu, L.-C. Cao and D.-B. Zhu, *Adv. Mater.*, **16**, 350 (2004).
- D.-L. Shi, J. Lian, W. Wang, G.-K. Liu, P. He, Z. Dong, L.-M. Wang and R.C. Ewing, *Adv. Mater.*, **18**, 189 (2006).
- Z.-M. Liu, J.-Q. Wang, J.-L. Zhang, B.-X. Han, Y. Wang and Z.-Y. Sun, *Micropor. Mesopor. Mater.*, **75**, 101 (2004).
- J.M.F.B. Aquino, A.S. Araujo, D.M.A. Melo, J.E.C. Silva, M.J.B. Souza and A.O.S. Silva, *J. Alloys. Compd.*, **374**, 101 (2004).
- J. Sauer, F. Marlow, B. Spliethoff and F. Schuth, *Chem. Mater.*, **14**, 217 (2002).
- Q. Cai, Z.-S. Luo, W.-Q. Pang, Y.-W. Fan, X.-H. Chen and F.-Z. Cui, *Chem. Mater.*, **13**, 258 (2001).
- M.S. Morey, S. O'Brien, S.S. War and, G.. D. Stucky, *Chem. Mater.*, **12**, 898 (2000).
- S. Sumiya, Y. Oumi, T. Uozumi and T. Sano, *J. Mater. Chem.*, **11**, 1111 (2001).
- Y. Han, X.-J. Meng, H.-B. Guan, Y. Yu, L. Zhao, X.-Z. Xu, X.-Y. Yang, S. Wu, N. Li and F.-S. Xiao, *Micropor. Mesopor. Mater.*, **57**, 191 (2003).
- Q.-S. Lu, Z.-Y. Wang, J.-G. Li, P.-Y. Wang and X.-L. Ye, *Nanoscale Res. Lett.*, **4**, 646 (2009).
- C.S. Cundy and J.-P. Zhao, *Chem. Commun.*, **14**, 1465 (1998).
- M. Park and S. Komarneni, *Micropor. Mesopor. Mater.*, **25**, 75 (1998).
- B.L. Newalkar, J. Olanrewaju and S. Komarneni, *J. Phys. Chem. B*, **105**, 8356 (2001).
- B.L. Newalkar, J. Olanrewaju and S. Komarneni, *Chem. Mater.*, **13**, 552 (2001).
- H. Yu and Q.-Z. Zhai, *Micropor. Mesopor. Mater.*, **123**, 298 (2009).
- J.C.P. Broekhoff and J.H. de Boer, *J. Catal.*, **10**, 368 (1968).
- S. Brumauer, P.H. Emmett and E. Teller, *J. Am. Chem. Soc.*, **60**, 309 (1938).
- E.P. Barrett, L.G. Joyner and P.P. Halenda, *J. Am. Chem. Soc.*, **73**, 373 (1951).
- H. Yu and Q.-Z. Zhai, *J. Solid. State. Chem.*, **181**, 2424 (2008).
- S. Sohrabnezhad, A. Pourahmad and M.A. Zanjanchi, *J. Iran. Chem. Soc.*, **6**, 612 (2009).
- J.R. Matos, L.P. Mercuri, J. Mietek, M. Kruk, Y. Sakamoto and O. Terasaki, *J. Mater. Chem.*, **11**, 2580 (2001).
- S. Brunauer, L.S. Deming, W.S. Deming, W.E. Deming and E. Teller, *J. Am. Chem. Soc.*, **62**, 1723 (1940).
- K.S.W. Sing, D.H. Everett, R.A.W. Haul, L. Moscou, R.A. Pierotti, J. Rouquerol and T. Siemieniowska, *Pure Appl. Chem.*, **57**, 603 (1985).
- M. Stocker, *Micropor. Mesopor. Mater.*, **82**, 257 (2005).
- J.-Q. Xu, W. Chu and S.-Z. Luo, *J. Mol. Catal. A*, **256**, 48 (2006).
- Q.-Z. Zhai and Y.-X. Liu, *Chin. J. Chem. Phys.*, **20**, 83 (2007).
- C. Pesquera, F. Gonzalez, C. Blanco and L. Sanchez, *Appl. Surf. Sci.*, **238**, 320 (2004).
- Y.-M. Luo, Z.-Y. Hou, R.-T. Li and X.-M. Zheng, *Micropor. Mesopor. Mater.*, **110**, 583 (2008).
- L. Vradman, M.V. Landau, D. Kantorovich, Y. Koltypin and A. Gedanken, *Micropor. Mesopor. Mater.*, **79**, 307 (2005).
- T. Abe, Y. Tachibana, T. Uematsu and M. Iwamoto, *Chem. Commun.*, **16**, 1617 (1995).
- H. Winkler, A. Birkner, V. Hagen, I. Worlf, R. Schmechel, H. von Seggern and R.A. Fischer, *Adv. Mater.*, **11**, 1444 (1999).
- W.-H. Zhang, J.-L. Shi, H.-R. Chen, Z.-L. Hua and D.-S. Yan, *Chem. Mater.*, **13**, 648 (2001).
- C.A. Kodaira, H.F. Brito, O.L. Malta and O.A. Serra, *J. Lumin.*, **101**, 11 (2003).
- Q.-H. Xu, L.-S. Li, B. Li, J.-H. Yu and R.-R. Xu, *Micropor. Mesopor. Mater.*, **38**, 351 (2000).
- Q.-H. Xu, L.-S. Fu, L.-S. Li, H.-J. Zhang, Q.-Q. Meng and R.-R. Xu, *Chin. Chem. Lett.*, **11**, 839 (2000).
- A.F. Kirby, D. Foster and F.S. Richardson, *Chem. Phys. Lett.*, **95**, 507 (1983).